Kinetics of Hydrocarbon Adsorption on Activated Carbon and Silica Gel

A. Malek and S. Farooq
Dept. of Chemical Engineering, National University of Singapore, Singapore 119260

Experimental breakthrough results of methane, ethane and propane in activated carbon and silica gel obtained over a wide range of gas compositions, bed pressures, interstitial velocities, and column temperatures were analyzed using a dynamic, nonisothermal, nontrace column breakthrough model. A linear driving force (LDF) approximation is used for particle uptake, and the Langmuir-Freundlich isotherm represents adsorption equilibrium. The LDF mass-transfer-rate coefficient (and, hence, effective particle diffusivity) and column-wall heat-transfer coefficient were determined. The results show that hydrocarbon transport in the activated carbon particles used is essentially by Knudsen and surface flow, while for the silica gel used the transport is primarily by Knudsen flow. For activated carbon, the experimentally derived LDF coefficients for all three sorbates are well correlated using an average effective diffusivity value. With regard to heat transfer, the column-wall Nusselt number is approximately constant for the range of Reynolds numbers considered. Simulations of multicomponent breakthrough in the activated-carbon bed based on independently measured single-component kinetic parameters and the extended Langmuir-Freundlich isotherm agree very well with experimental results. The computational efficiency gained by adopting the simpler extended Langmuir isotherm model is also investigated.

Introduction

The reliability of an adsorption-process model largely depends on the adequacy of its constituent models, which represent equilibrium isotherm, mass-transfer, and heat-transfer dynamics. While extensive studies over the years have verified general qualitative similarities in the equilibrium and kinetic behavior of various commonly used systems, such as hydrocarbon adsorption on activated carbon and silica gel, these studies have also revealed significant differences in the measured data due to microscopic variations in samples of the same type of adsorbent resulting from a difference in the manufacturing procedure. Quantitative generalization is therefore practically impossible with the present state of knowledge. Thus, the equilibrium and mass-transfer behavior of a given sorbate–sorbent system are normally established from independent experiments and constitute an integral part of a process modeling study.

In a recent article (Malek and Farooq, 1996), we reviewed a number of the more important isotherm models in the context of modeling the equilibrium data of methane, ethane, and propane in activated carbon, with the ultimate objective of developing a multibed, multicomponent PSA simulation model for hydrogen purification from refinery fuel gas. Equilibrium data reported in that article were obtained by the dynamic-column breakthrough (DCBT) method, which was detailed in two other publications (Malek et al., 1995; Malek and Farooq, 1996a). Similar breakthrough studies have also been conducted in a silica gel bed (Malek, 1996). In this article, the profiles of the dynamic-column breakthrough experiments are analyzed to derive mass-transfer- as well as heat-transfer-rate data for the adsorption of methane, ethane, and propane in activated-carbon and silica-gel particles. With regard to adsorption-column dynamics, numerous models of the breakthrough process, of differing model complexity, have been introduced (Ruthven, 1984). The simplest form of the breakthrough model is an isothermal plug-flow trace-component system, with a linear-equilibrium isotherm equation. In this study, a nonisothermal, axially dispersed plug-flow model is adopted. The Langmuir-Freundlich isotherm model is used

Correspondence concerning this article should be addressed to S. Farooq.

to represent the equilibrium relationship, and the linear driving force (LDF) approximation is used to represent particle uptake.

It is shown that the DCBT method provides a simple and practically useful way of extracting the mass- and heat-transfer-rate parameters for the present systems. In addition, the parameters determined from single-component breakthrough studies can successfully predict multicomponent breakthrough behavior under different operating conditions.

Theory

The mathematical model of a nonisothermal, dynamic-column adsorption breakthrough process is basically a transient material and energy balance. In this regard, both the adsorption equilibrium and kinetic aspects of the process must be accounted for. The model adopted here utilizes the Langmuir-Freundlich equilibrium isotherm equation and a linear driving force (LDF) rate model. The LDF model is a lumped-parameter model for particle adsorption. In this study, a constant LDF mass-transfer coefficient is used, in contrast to the modified, variable LDF coefficient as introduced by Vermeulen (1953) and Vermeulen and Quilici (1970). Hence, the simulation problem is reduced to the simple task of determining the LDF coefficient, k. This approach is particularly beneficial since the ultimate objective of this study is to model a multibed, multicomponent pressure-swing adsorption process for hydrogen purification from refinery fuel gas, which can be expected to be computationally demanding. Moreover, this is an equilibrium-controlled process for which it would be adequate to represent particle mass-transfer kinetics using a lumped-parameter model (Ruthven et al., 1994). Although it would be possible to adopt a variable LDF coefficient or a distributed-parameter model for particle adsorption, these approaches are likely to incur too large a computational workload without any significant gain in the quality of prediction.

A general model for a single-adsorbate, nonisothermal, isobaric, and variable-velocity process follows. For both material and thermal-energy balances, axially dispersed plug flow is assumed, with no radial gradients. For material balance, the assumption of negligible radial gradient is valid since the column length-to-diameter ratio is very large ($(L/2R_B) > 10$). For energy balance, this assumption is valid since for the present system, $(K_r L/[v_f R_i^2 (C_p)_g \rho_g \epsilon_B])$ is relatively large (≈ 5). Farooq and Ruthven (1990) have shown that for large values (> 3) of this ratio, the radial temperature gradient in the packed bed is essentially negligible. In the present study, however, an effective temperature gradient is assumed between the packed bed and the column wall. The temperatures of gas and particle are assumed to be the same at each point in the column. For relatively small particles and high gas velocity, the particle heat-transfer resistance is negligible, and hence the latter assumption is valid. Furthermore, because a high flow rate of water is used in the outer jacket of the column, wall-temperature fluctuations can be expected to be negligible. This point is verified in a later section relating to heat-transfer data analysis. Thus, for heat-transfer considerations, only the apparent heat-transfer coefficient between the wall and the bed, h_w, needs to be approximated from the experimental temperature breakthrough data.

The nondimensional form of the breakthrough model equations are presented here. A detailed derivation of these dimensionless equations from more elementary material and energy balances are shown in the Appendix. For the adsorption of a sorbate from an inert carrier in a packed bed of adsorbent, the nondimensional, transient-component, and overall material balances in the column are given by

$$\frac{\partial X_a}{\partial \tau} = \frac{1}{P_{em}}\left(\frac{\partial^2 X_a}{\partial \chi^2} - \frac{2}{\theta}\frac{\partial X_a}{\partial \chi}\frac{\partial \theta}{\partial \chi}\right) - V\frac{\partial X_a}{\partial \chi} + \varphi\gamma_a(X_a - 1)\frac{\partial Y_a}{\partial \tau} \quad (1)$$

$$\frac{\partial V}{\partial \chi} = \frac{1}{P_{em}}\left(\frac{2}{\theta^2}\left(\frac{\partial \theta}{\partial \chi}\right)^2 - \frac{1}{\theta}\frac{\partial^2 \theta}{\partial \chi^2}\right) + \frac{1}{\theta}\frac{\partial \theta}{\partial \tau} + \frac{V}{\theta}\frac{\partial \theta}{\partial \chi} - \varphi\gamma_a\frac{\partial Y_a}{\partial \tau}. \quad (2)$$

The axial derivatives of temperature appear in the preceding equations due to the dependence of gas volume on the local column temperature. The ideal gas law has been assumed in deriving these equations. In the experiments conducted, a back-pressure regulator was used to maintain a constant system pressure. Axial pressure drop in the bed is also negligible. Since this is a "closed-closed" system, the Danckwerts boundary conditions are applicable for the component balance:

$$\left.\frac{\partial X_a}{\partial \chi}\right|_{\chi=0} = -P_{em}(X_a|_{\chi=0^-} - X_a|_{\chi=0^+}) \quad (3a)$$

$$\left.\frac{\partial X_a}{\partial \chi}\right|_{\chi=1} = 0. \quad (3b)$$

The boundary condition for the overall material balance is given by

$$V(0,\tau) = 1. \quad (4)$$

An energy balance for the system, with axial thermal conduction and constant wall temperature, yields

$$\frac{\partial \theta}{\partial \tau} = \left(\frac{1}{P_{eh}} + \frac{\phi_1}{P_{em}}\right)\frac{\partial^2 \theta}{\partial \chi^2} - \phi_1 V\frac{\partial \theta}{\partial \chi} - \frac{2\phi_1}{P_{em}}\frac{1}{\theta}\left(\frac{\partial \theta}{\partial \chi}\right)^2 + \phi_1\varphi\gamma_a(\theta + \zeta_a)\frac{\partial Y_a}{\partial \tau} - \phi_2(\theta - \theta_w). \quad (5)$$

If the wall temperature is constant and equal to that of feed, then $\theta_w = 1.0$. The following boundary conditions, analogous to the familiar Danckwerts boundary conditions, are applied for the heat balance:

$$\left.\frac{\partial \theta}{\partial \chi}\right|_{\chi=0} = -P'_{eh}(\theta|_{\chi=0^-} - \theta|_{\chi=0^+}) \quad (6a)$$

$$\left.\frac{\partial \theta}{\partial \chi}\right|_{\chi=1} = 0. \quad (6b)$$

Equation 2 is first order in the velocity derivative, and hence requires only one boundary condition for computing the velocity profile. In this case, the Dirichlet boundary condition is used at $\chi = 0$, since the value is known. It is interesting to note that the use of the Danckwerts boundary condition for mass and heat transfer forces $\partial Y_a/\partial\tau$ to be zero at both $\chi = 0^+$ and $\chi = 1^-$, since that boundary condition assumes negligible source or sink terms at $\chi = 0^+$ and $\chi = 1^-$. Thus, at $\chi = 1$, Eq. 2 is reduced to $\partial V/\partial\chi = 0$, which provides an extraneous boundary condition at that point. If pressure varies, as in pressure-swing adsorption modeling, then this additional condition at $\chi = 1$ is not applicable.

For particle uptake, the LDF mass-transfer-rate model is given as follows:

$$\frac{\partial Y_a}{\partial\tau} = \alpha_a(Y_a^* - Y_a). \tag{7}$$

The equilibrium adsorption capacity, Y_a^*, in turn, is given by the equilibrium adsorption isotherm. In this study, the Langmuir-Freundlich equilibrium isotherm model is used since it provides a very good fit of experimental equilibrium data over a wide range of pressures and temperatures (Malek and Farooq, 1996b; Malek, 1996). The isotherm equation is given as follows:

$$Y_a^* = \frac{\beta_a X_a^{na}}{1 + \beta_a X_a^{na}}, \tag{8}$$

where

$$\beta_a = b_{oa}\exp\left(\frac{(-\Delta H_A)_a}{RT_f}\frac{1}{\theta}\right)P_f^{na}.$$

It is important to note that the Langmuir-Freundlich model is not thermodynamically consistent, in the sense that $\partial q^*/\partial P_a$ does not approach a constant value in the limit as $P_a \to 0$. Numerically, this is an important characteristic insofar as the breakthrough profiles at low pressures are concerned. When this property is absent, the adsorption and desorption profiles obtained using the Langmuir-Freundlich isotherm model in the linear range of the isotherm (i.e., at very low pressures) are expected to be asymmetric, as opposed to experimentally observed symmetry in this range. However, for the systems being studied, the thermodynamically consistent models provide less satisfactory fit of experimental equilibrium data over the entire range covered here (Malek and Farooq, 1996b; Malek, 1996). Hence, the impact of the asymmetry in the linear range on the extracted mass-transfer parameter using the Langmuir-Freundlich model is likely to be less detrimental than the impact of choosing a thermodynamically consistent isotherm model that offers a less satisfactory representation of the equilibrium solid loading.

The following initial conditions apply to the bed, depending on whether the simulation is for adsorption from a regenerated bed or for desorption from a saturated bed:

Adsorption

$$X_a(\chi,0) = 0 \qquad Y_a(\chi,0) = 0. \tag{9a}$$

Desorption

$$X_a(\chi,0) = X_{ao} \qquad Y_a(\chi,0) = Y_a^*(X_{ao}). \tag{9b}$$

In all cases, $\theta(\chi,0) = 1.0$.

Estimation of Model Parameters

Apart from k and h_w, the other model parameters constituting the various dimensionless groups in Eqs. 1–8 were either measured or determined empirically. The axial dispersion coefficient, D_L, was determined from the following correlation given by Edwards and Richardson (1968):

$$\frac{1}{P_e} = \frac{g_1\epsilon_B}{ReSc} + \frac{1}{P_e'\left(1 + \dfrac{g_1 g_2 \epsilon_B}{ReSc}\right)}. \tag{10}$$

It should be noted that the correlation just given is for a Peclet number that is based on particle diameter, whereas for Eqs. 1, 2, and 3a, the mass-transfer Peclet number definition is based on the column length. For the adsorption system considered here, the following values of the constants were used:

$$g_1 = 0.73$$

$$g_2 = 13.0$$

$$P_e' = 2.0.$$

The fluid-phase mass-transfer coefficient, k_f, was calculated from the following correlation given by Wakao and Funazkri (1978):

$$Sh = 2.0 + 1.1\,Sc^{1/3}Re^{0.6}. \tag{11}$$

For the energy equation, the effective axial thermal conductivity, K_z, which appears in the thermal Peclet numbers, P_{eh} and P'_{eh}, can be estimated using the empirical correlation given by Kunii and Smith (1960) and Yagi et al. (1960) as follows:

$$K_z = K_{z0} + K_g\delta PrRe \tag{12a}$$

$$K_{z0} = K_g\left(\epsilon_B + \frac{1-\epsilon_B}{\psi + 2/3(K_g/K_p)}\right) \tag{12b}$$

$$\psi = \psi_2 + (\psi_1 - \psi_2)\left(\frac{\epsilon_B - 0.26}{0.216}\right). \tag{12c}$$

For all the simulations conducted in this study, the following parameter values were adopted (Suzuki, 1990):

$$\delta = 0.75$$

$$\psi_1 = 0.1$$

$$\psi_2 = 0.07.$$

Gas viscosity and thermal conductivity in the column were calculated as a mixture of inert carrier and the sorbate, using

the semiempirical formulas of Wilke (Bird et al., 1960). The gas density and specific heat capacity were calculated based on a weighted average of carrier and sorbate.

Determination of Mass- and Heat-Transfer Coefficients

The mass-transfer coefficient, k (in α_a), and the heat-transfer coefficient, h_w (in ϕ_2), are the two remaining unknowns that were used as adjustable parameters in fitting the simulation breakthrough profiles with experimental profiles. These variables were determined iteratively by ensuring a good fit of the simulation to experimental data. At least two experimental measurements or profiles are required for an unambiguous determination of the two unknowns. These are the concentration and temperature breakthrough profiles. The adsorption- and desorption-concentration breakthrough profiles were simultaneously matched to improve the reliability of the mass-transfer coefficient. The reliability of the wall-heat transfer coefficient was similarly improved by matching the temperature profiles measured at two points in the bed.

The individual mass-transfer resistances for a biporous, spherical adsorbent are related to the LDF mass-transfer coefficient by the following equation:

$$\frac{1}{k} = \frac{R_p}{3k_f}\frac{q^*\rho_p}{C_{af}} + \frac{R_p^2}{15\epsilon_p D_e}\frac{q^*\rho_p}{C_{af}} + \frac{R_c^2}{15D_c} \tag{13}$$

which, for negligible micropore resistance, reduces to

$$\frac{1}{k} = \frac{R_p}{3k_f}\frac{q^*\rho_p}{C_{af}} + \frac{R_p^2}{15\epsilon_p D_e}\frac{q^*\rho_p}{C_{af}}. \tag{13a}$$

The effective diffusivity, D_e, in turn, is related to molecular, Knudsen, and surface diffusivities as follows:

$$\frac{1}{D_e} = \frac{\tau_p}{D_m} + \frac{1}{\dfrac{D_k}{\tau_p} + \dfrac{1-\epsilon_p}{\epsilon_p}\left(\dfrac{q^*\rho_p}{C_{af}}\right)\dfrac{D_s}{\tau_s}}. \tag{14}$$

The molecular diffusivity, D_m, required in Eq. 11 to calculate the Sherwood number, Sh, as well as in Eq. 14, was calculated using the Chapman-Enskog equation (Bird et al., 1960). The Knudsen diffusivity, D_k, is estimated using the following equation (Karger and Ruthven, 1986):

$$D_k = 9{,}700 r_{po}\sqrt{\frac{T}{M}}. \tag{15}$$

Using the value of k found for each breakthrough run, the effective diffusivity was determined from Eq. 13a. Experimental evidence of negligible micropore resistance is discussed later. The effective diffusivity, D_e, thus obtained was then used in Eq. 14 to determine the magnitude of surface diffusivity. It should be mentioned that, in the absence of reliable information, the pore tortuosity, τ_p, and surface tortuosity, τ_s, can be taken as equal (Huang and Fair, 1988).

Numerical Solution

The dynamic equations for gas-phase concentration, solid-phase concentration, gas velocity, as well as bed temperature given earlier were solved simultaneously to simulate the breakthrough profiles. The preferred means of numerically solving this complicated set of partial differential equations is to use orthogonal collocation to discretize the equations (Finlayson, 1972; Raghavan and Ruthven, 1983). The discretization was done for the spatial variable, resulting in a set of time-derivative ODEs for the sorbate concentration and bed temperature. The overall material balance was converted to a set of linear algebraic equations in order to solve for the gas velocity in the bed. In this study, a total of 19 collocation points were chosen in order to provide reasonable representations of the sharp concentration and temperature waves traveling down the column. Details of the collocation form of the system of equations, as well as the solution scheme, are discussed elsewhere (Malek, 1996).

The set of ODEs will be stiff, since the equilibrium isotherm for hydrocarbon adsorption in activated carbon is significantly nonlinear. Hence, they were solved using an implicit backward differentiation formula. The linear algebraic equations arising from the discretized overall material balance was efficiently solved using LU-decomposition (Press et al., 1992). The breakthrough model developed here was solved on a personal computer using a Salford FORTRAN Compiler in double precision.

Results and Discussion

In this study, breakthrough experiments of methane, ethane, and propane in activated carbon and silica gel beds were determined for three different temperatures, two particle sizes as well as various gas interstitial velocities and bed pressures. The experimental apparatus, procedure, and analysis of the dynamic column breakthrough experiments have been detailed in earlier publications (Malek et al., 1995; Malek and Farooq, 1996a). Table 1 provides some relevant data on the adsorbents used as well as other information regarding the experiments conducted. The equilibrium isotherm parameters used in the simulations are given in Table 2.

As a prelude to the kinetic analysis, some simulations were conducted to study the characteristics of the dynamic breakthrough model used here. Equations 1, 2 and 5 portray the full nonisothermal material and energy-balance equations for fixed-bed adsorption. However, it was found that some of the derivative terms were generally insignificant due to their relatively small magnitude. Based on a number of simulations conducted for various feed velocities, temperatures, and bed pressures, the following simplified versions of the model equations, which are applicable to all three hydrocarbon adsorptions on both activated-carbon and silica gel, were found to be adequate:

Component material balance:

$$\frac{\partial X_a}{\partial \tau} = \frac{1}{P_{em}}\frac{\partial^2 X_a}{\partial \chi^2} - V\frac{\partial X_a}{\partial \chi} + \varphi\gamma_a(X_a - 1)\frac{\partial Y_a}{\partial \tau}. \tag{1a}$$

Table 1. Properties of Adsorbent and Other Experimental Information

Column	*Jacketed stainless steel*
Internal diameter:	3.5 cm
Length:	40.0 cm
Adsorbent	*Activated Carbon*
Apparent density:*	0.87 g cm^{-3}
Particle porosity:*	0.58
Mean pore radius:*	18×10^{-8} cm (18 Å)
Specific surface area:*	970 m^2 g^{-1}
Particle heat capacity:**	0.95 J/g K
Particle Sizes:	(a) Column 1: 2.36–2.80 mm (Tyler Equiv. 8-mesh and 7-mesh)
	(b) Column 2: 1.18–1.40 mm (Tyler Equiv. 16-mesh and 14-mesh)
Bed void fraction:	(a) Column 1: 0.3994
	(b) Column 2: 0.4180
Adsorbent	*Silica Gel*
Apparent density:*	1.15 g cm^{-3}
Particle porosity:*	0.44
Mean pore radius:*	20×10^{-8} cm (20 Å)
Specific surface area:*	666 m^2 g^{-1}
Particle heat capacity:**	0.92 J/g K
Particle Sizes:	(a) Column 1: 2.36–2.80 mm (Tyler Equiv. 8-mesh and 7-mesh)
Bed void fraction:	(a) Column 1: 0.3612
Adsorbate	Methane (100.0%)
	Ethane (100.0%)
	Propane (99.5%, ethane remainder)
Carrier:	Helium
Experimental range	
Interstitial gas velocity	1.3 to 4.3 cm/s
Pressure	1.99 to 6.41 bar
Temperature	299.15 to 338.15 K

*Experimentally measured in this laboratory. Mean pore radius and specific surface area were determined using mercury porosimetry.
**Approximated based on Perry's *Chemical Engineers' Handbook*, 6th ed., McGraw-Hill, New York, 1984.

Overall material balance:

$$\frac{\partial V}{\partial \chi}=\frac{1}{P_{em}}\frac{2}{\theta^2}\left(\frac{\partial \theta}{\partial \chi}\right)^2+\frac{V}{\theta}\frac{\partial \theta}{\partial \chi}-\varphi\gamma_a\frac{\partial Y_a}{\partial \tau}. \qquad (2a)$$

Thermal-energy balance:

$$\frac{\partial \theta}{\partial \tau}=\frac{1}{P_{eh}}\frac{\partial^2\theta}{\partial \chi^2}-\phi_1 V\frac{\partial \theta}{\partial \chi}+\phi_1\varphi\gamma_a(\theta+\zeta_a)\frac{\partial Y_a}{\partial \tau}-\phi_2(\theta-\theta_w). \qquad (5a)$$

Table 2. Langmuir-Freundlich and Langmuir Isotherm Model Parameters for Hydrocarbon Adsorption in Activated Carbon† and Silica Gel**

	Activated Carbon		Silica Gel	
		Langmuir-Freundlich Isotherm		
Methane	$q_s^*=7.3304$ $b_{ao}=1.99\times10^{-4}$	$-\Delta H_A=15.95\times10^3$ na = 0.9169	$q_s^*=2.3310$ $b_{ao}=5.23\times10^{-4}$	$-\Delta H_A=11.97\times10^3$ na = 0.949
Ethane	$q_s^*=7.6364$ $b_{ao}=1.44\times10^{-3}$	$-\Delta H_A=15.17\times10^3$ na = 0.6590	$q_s^*=1.77$ $b_{ao}=5.27\times10^{-5}$	$-\Delta H_A=23.11\times10^3$ na = 0.899
Propane	$q_s^*=4.8416$ $b_{ao}=3.21\times10^{-3}$	$-\Delta H_A=17.45\times10^3$ na = 0.6285	$q_s^*=10.10$ $b_{ao}=2.03\times10^{-4}$	$-\Delta H_A=16.62\times10^3$ na = 0.815
		Langmuir Isotherm		
Methane	$q_s^*=5.8243$ $b_{ao}=1.92\times10^{-4}$	$-\Delta H_A=16.63\times10^3$	$q_s^*=1.7601$ $b_{ao}=5.05\times10^{-4}$	$-\Delta H_A=12.80\times10^3$
Ethane	$q_s^*=5.4738$ $b_{ao}=5.61\times10^{-5}$	$-\Delta H_A=25.10\times10^3$	$q_s^*=1.611$ $b_{ao}=2.34\times10^{-5}$	$-\Delta H_A=25.61\times10^3$
Propane	$q_s^*=3.7348$ $b_{ao}=4.11\times10^{-4}$	$-\Delta H_A=26.44\times10^3$	$q_s^*=3.7646$ $b_{ao}=1.84\times10^{-4}$	$-\Delta H_A=20.12\times10^3$

Note: refer to Notation for units.
†Malek and Farooq (1996b).
**Malek (1996).

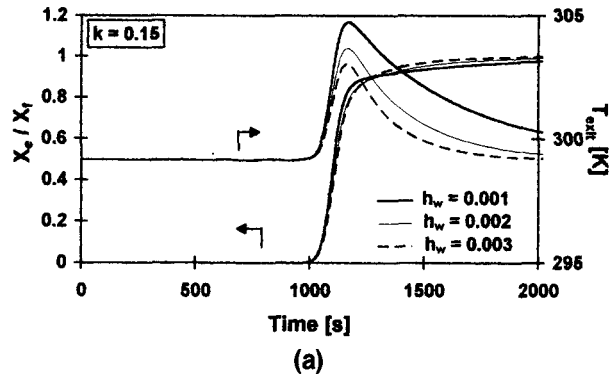

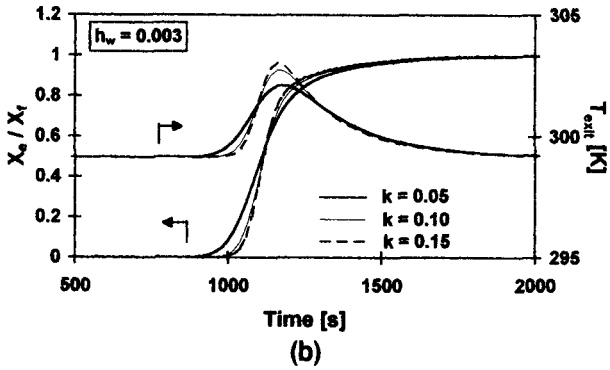

Figure 1. (a) Effect of wall heat-transfer coefficient, h_w [J/cm^2·s·K], on the concentration and temperature breakthrough profiles; (b) effect of LDF rate coefficient, k[s^{-1}], on the concentration and temperature breakthrough profiles.

It should be noted that a similar simplification of the adsorption model has also been reported by other workers (Tsai et al., 1983). Any further simplification in the model equations results in a noticeable deviation from the full model.

A second set of simulation runs was conducted to determine the effect of k on heat-transfer dynamics, as well as the effect of h_w on mass-transfer dynamics. Figure 1 shows the exit concentration and temperature profiles obtained using different values of k and h_w. The equilibrium model parameters used in the runs are the Langmuir-Freundlich isotherm parameters for methane adsorption in activated carbon. An interesting observation is that a major portion of the concentration breakthrough profile is essentially unaffected by a large variation in the apparent wall-heat-transfer coefficient, while the mass-transfer coefficient has a noticeable effect on both the concentration breakthrough profile and the column-temperature profile. However, the temperature profile is more sensitive to the wall-heat-transfer coefficient than the mass-transfer coefficient. This observation can be explained by the fact that the mass-transfer front has a higher natural velocity in the bed than does the thermal front, since the activated carbon particles have a large specific heat capacity (Farooq and Ruthven, 1990). Under this condition, it is possible to obtain unambiguous values of both the mass- and heat-transfer coefficients from experimental breakthrough curves by first fitting the concentration profile for k, and then fitting the temperature profile for h_w.

These preliminary studies provided valuable information in selecting the best means of determining reliable k and h_w values from experimental breakthrough runs. Figure 2 shows a representative fit of theoretical concentration and temperature profiles with experimental data.

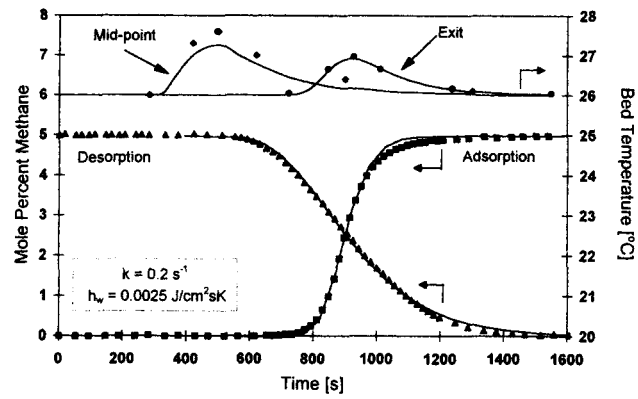

Figure 2. Concentration and temperature breakthrough curves for methane in activated carbon at 299.15°C.

Symbols, experimental; lines, simulations.

Kinetic data for hydrocarbon adsorption in activated carbon (HC-AC)

Figure 3a shows the values of the LDF mass-transfer coefficients obtained from the single-component breakthrough results for methane, ethane, and propane single-component adsorption in activated carbon as a function of the ratio of equilibrium-adsorbed amount to feed concentration, $q^*\rho_p/C_{af}$, on a semilog plot. These results were obtained for various total gas pressures, interstitial velocities and column temperatures as detailed in Table 3. The k values for the three hydrocarbons indicate a consistent, monotonically decreasing trend with increasing equilibrium constant (i.e., increasing trend with gas concentration). Of particular interest is that, for the operating conditions studied here, the k values for the three gases generally fall within a narrow band, except for some high-concentration results for propane adsorption. It would be interesting to further investigate the controlling diffusion mechanism in the adsorbent particles for the adsorption of the three hydrocarbons.

In some of the experiments conducted, smaller particles were used in order to determine the significance of micropore mass-transfer resistance. It was found that the mass-transfer coefficient is approximately inversely proportional to the square of the particle diameter, thus confirming that the mass transfer is indeed controlled by diffusion in the macropore (Runs 1–3 and 1a–3a, for methane; Runs 4 and 4a for ethane in Table 3). Referring to Eq. 13, if micropore resistance is controlling and the external film resistance is small (the latter is verified in another section), then changing the size of the particle would have little effect on the LDF mass-transfer coefficient. Indeed, Hu and Do (1993) suggested that micropore resistance is negligible for large activated-carbon particles (with diameter > 2 mm), while it can be appreciable for small particles (with diameter < 1.5 mm). Thus, the results obtained here seem to corroborate the findings of Hu and Do (1993).

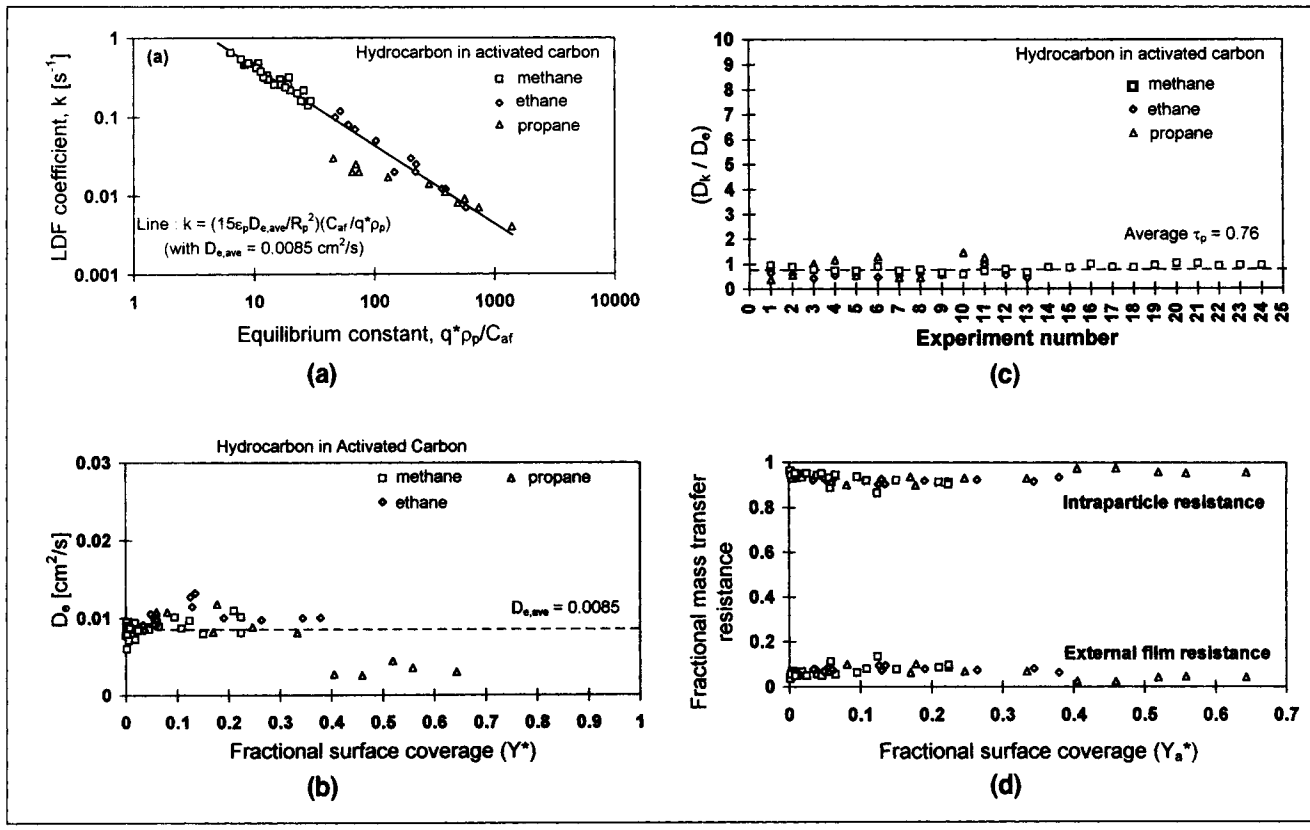

Figure 3. Mass-transfer kinetics of hydrocarbons in activated carbon: (a) variation of LDF rate coefficient, k, with equilibrium constant; (b) variation of effective diffusivity, D_e, with surface coverage, Y_a; (c) (D_k/D_e) ratio for all the runs; (d) fraction of total particle mass-transfer resistance due to external film and intraparticle diffusion.

Experimental details are given in Tables 1 and 3.

Figure 3b shows the variation of the effective diffusivity, D_e, calculated using Eq. 13a, as a function of surface coverage for the hydrocarbons in activated carbon. For methane and ethane adsorption in activated carbon, there is no systematic variation in the effective diffusivity within the range of operating conditions considered here. However, there is some observable variation of the effective diffusivity with surface coverage for propane adsorption. The existence of surface diffusion for the HC-AC system is demonstrated in Figure 3c. Here, the ratio (D_k/D_e) calculated using the experimental D_e values are plotted. For the activated carbon particles as well as silica gel particles used, the mean pore radius is relatively small, and hence pore flux is controlled primarily by Knudsen diffusion. Therefore, referring to Eq. 14, for negligible flux due to surface diffusion in the particles (i.e., $D_s \approx 0$), this ratio is essentially an estimate of the particle tortuosity, τ_p. As can be seen from Figure 3c, this approximation yields tortuosity values that are too small for the highly porous activated carbon. This indicates that, in addition to Knudsen flow, there is an additional flux from surface diffusion for the HC-AC system.

In recent publications related to hydrocarbon adsorption on activated carbon, it has been widely accepted that intraparticle diffusion in the pores is predominantly through a combination of Knudsen diffusion, D_k, and surface diffusion, D_s (Doong and Yang, 1986; Huang and Fair, 1988). The effective particle diffusivity for a combination of Knudsen and surface diffusion is defined as

$$D_e = \left(\frac{1}{\tau_p}\right)\left[D_k + \frac{1-\epsilon_p}{\epsilon_p}\left(\frac{q^*\rho_p}{C_{af}}\right)D_s\right]. \qquad (14a)$$

It should be realized, however, that in order to determine D_s, the particle tortuosity should be known. Table 3 shows the estimated surface diffusivity, as well as other relevant diffusivities for the experimental runs conducted using an approximate particle tortuosity of 4.0.

The calculated D_s values, as shown in Table 3, generally increase with increasing surface coverage, as expected (Kapoor et al., 1989). It is important to note, however, that these values have been extracted from an integral-step breakthrough run using the LDF model. As a result, the concentration dependence of D_s is likely to have been somewhat attenuated (Garg and Ruthven, 1972, 1975). On the other hand, for the nonlinear adsorption isotherm, the equilibrium constant $(q^*\rho_p/C_{af})$ decreases with increasing surface coverage. Hence, whether the effective diffusivity will increase, decrease, or remain constant will depend on the relative magnitude of the two opposing changes mentioned earlier.

Table 3. Experimental and Calculated Mass-transfer Parameters for Hydrocarbon Adsorption on Activated Carbon*

Run No.	T K	d_p** cm	X_f	Pres. bar	v_f cm/s	D_m cm²/s	D_k cm²/s	k s⁻¹	D_e cm²/s	D_s ($\tau_p = 4.0$) cm²/s
						Methane				
1	299.15	0.258	0.006	1.9943	1.50	0.346	7.550E−03	0.140	7.848E−03	1.330E−03
2	299.15	0.258	0.010	3.4167	1.69	0.202	7.550E−03	0.160	8.138E−03	1.748E−03
3	299.15	0.258	0.050	2.4848	1.56	0.278	7.550E−03	0.200	9.411E−03	2.167E−03
4	299.15	0.258	0.194	2.3867	1.61	0.289	7.550E−03	0.260	1.025E−02	2.893E−03
5	299.15	0.258	0.399	2.2886	1.62	0.302	7.550E−03	0.300	1.010E−02	3.272E−03
6	299.15	0.258	0.600	4.9373	1.63	0.140	7.550E−03	0.320	8.044E−03	3.941E−03
7	299.15	0.258	0.180	6.5070	1.48	0.106	7.550E−03	0.260	9.662E−03	4.378E−03
8	299.15	0.258	0.011	2.9753	2.85	0.232	7.550E−03	0.160	9.502E−03	1.805E−03
9	299.15	0.258	0.624	5.3787	2.71	0.128	7.550E−03	0.450	1.011E−02	6.707E−03
10	299.15	0.258	0.005	1.9943	4.21	0.346	7.550E−03	0.160	9.468E−03	1.632E−03
11	299.15	0.258	0.620	4.9373	4.23	0.140	7.550E−03	0.480	1.096E−02	7.137E−03
12	318.15	0.258	0.005	1.9943	1.50	0.383	7.786E−03	0.220	8.819E−03	2.145E−03
13	318.15	0.258	0.010	3.3677	1.72	0.227	7.786E−03	0.240	8.991E−03	2.651E−03
14	318.15	0.258	0.052	2.4848	1.56	0.308	7.786E−03	0.260	7.708E−03	2.487E−03
15	318.15	0.258	0.207	2.4848	1.55	0.308	7.786E−03	0.340	8.826E−03	3.462E−03
16	318.15	0.258	0.417	2.4848	1.50	0.308	7.786E−03	0.420	8.934E−03	4.293E−03
17	318.15	0.258	0.620	4.9373	1.63	0.155	7.786E−03	0.460	7.927E−03	5.338E−03
18	338.15	0.258	0.005	1.9943	1.50	0.425	8.027E−03	0.300	7.745E−03	2.697E−03
19	338.15	0.258	0.011	3.3677	1.72	0.251	8.027E−03	0.320	7.787E−03	3.168E−03
20	338.15	0.258	0.052	2.4848	1.56	0.341	8.027E−03	0.380	8.719E−03	3.734E−03
21	338.15	0.258	0.200	2.4848	1.55	0.341	8.027E−03	0.480	8.409E−03	4.650E−03
22	338.15	0.258	0.418	2.4848	1.50	0.341	8.027E−03	0.540	8.471E−03	5.241E−03
23	338.15	0.258	0.615	4.9373	1.63	0.171	8.027E−03	0.650	8.645E−03	7.614E−03
24	338.15	0.258	0.180	6.4090	1.51	0.132	8.027E−03	0.480	9.311E−03	6.728E−03
1a	299.15	0.129	0.005	1.9943	1.51	0.346	7.550E−03	0.450	6.741E−03	9.985E−04
2a	299.15	0.129	0.010	3.3677	1.70	0.205	7.550E−03	0.480	6.780E−03	1.191E−03
3a	299.15	0.129	0.050	2.4848	1.56	0.278	7.550E−03	0.620	7.468E−03	1.510E−03
						Ethane				
1	299.15	0.258	0.004	2.4848	1.33	0.211	5.514E−03	0.007	8.382E−03	8.231E−05
2	299.15	0.258	0.010	2.4848	1.32	0.211	5.514E−03	0.012	9.204E−03	1.473E−04
3	299.15	0.258	0.050	1.9943	1.28	0.263	5.514E−03	0.030	1.275E−02	3.974E−04
4	299.15	0.258	0.367	2.4848	1.30	0.211	5.514E−03	0.080	9.992E−03	1.010E−03
5	299.15	0.258	0.010	2.4848	3.61	0.211	5.514E−03	0.012	9.788E−03	1.493E−04
6	299.15	0.258	0.046	1.9943	3.57	0.263	5.514E−03	0.025	1.149E−02	3.115E−04
7	318.15	0.258	0.010	2.4848	1.32	0.235	5.686E−03	0.020	9.127E−03	2.359E−04
8	318.15	0.258	0.188	2.4848	1.31	0.235	5.686E−03	0.070	1.005E−02	8.571E−04
9	318.15	0.258	0.379	2.4848	1.30	0.235	5.686E−03	0.100	9.782E−03	1.205E−03
10	338.15	0.258	0.011	2.4848	1.32	0.260	5.862E−03	0.020	5.900E−03	1.891E−04
11	338.15	0.258	0.043	1.9943	1.29	0.323	5.862E−03	0.050	1.056E−02	5.739E−04
12	338.15	0.258	0.187	2.4848	1.31	0.260	5.862E−03	0.120	1.325E−02	1.607E−03
4a	299.15	0.129	0.395	2.4848	1.30	0.211	5.514E−03	0.280	8.911E−03	8.423E−04
						Propane				
1	299.15	0.258	0.009	1.9943	1.99	0.213	4.553E−03	0.004	1.179E−02	4.249E−05
2	299.15	0.258	0.045	1.9943	2.00	0.213	4.553E−03	0.008	8.072E−03	7.803E−05
3	299.15	0.258	0.213	2.4848	1.99	0.171	4.553E−03	0.017	4.395E−03	1.389E−04
4	299.15	0.258	0.251	4.5453	1.95	0.094	4.553E−03	0.020	2.971E−03	1.362E−04
5	318.15	0.258	0.045	1.9943	1.99	0.238	4.695E−03	0.011	8.793E−03	1.083E−04
6	318.15	0.258	0.252	4.4468	1.99	0.107	4.695E−03	0.025	3.505E−03	1.842E−04
7	338.15	0.258	0.006	1.9943	1.31	0.264	4.840E−03	0.007	1.083E−02	7.180E−05
8	338.15	0.258	0.009	2.4848	1.32	0.212	4.840E−03	0.009	1.078E−02	9.382E−05
9	338.15	0.258	0.045	1.9943	1.28	0.264	4.840E−03	0.014	8.136E−03	1.345E−04
10	338.15	0.258	0.354	2.9753	1.31	0.177	4.840E−03	0.020	2.555E−03	1.142E−04
11	338.15	0.258	0.447	2.9753	1.32	0.177	4.840E−03	0.030	2.679E−03	1.784E−04

*Adsorbent physical properties are given in Table 2, column one. Other experimental details are given in Table 2, column 2.
**Particle size is mean of two Tyler Equivalent Mesh sizes (refer to Table 2, column 2).

Surface diffusion is an activated process with an activation energy, $(-\Delta H_s)$, and is a function of the surface coverage, Y_a (Kapoor et al., 1989), which can be attributed to isotherm nonlinearity by taking chemical potential gradient as the driving force. For the Langmuir-Freundlich isotherm model, the surface diffusivity is given by

$$D_s = \frac{D_{so}}{(1-Y_a)^{na}} \exp\left(\frac{(-\Delta H_s)}{RT}\right). \tag{16}$$

Figure 4 shows semilog plots of $D_s(1-Y_a)^{na}$ against $1/T$. The linearity of these plots with nonzero gradients is indicative of the fact that the additional flux is due to an activated process. The calculated activation energy for each hydrocarbon is approximately the same, as shown in the figures. The magnitude of the activation energy for the surface diffusion is also smaller than the respective heat of adsorption, $(-\Delta H_A)$, as expected (refer to Table 2). This analysis provides further verification that the additional flux observed for hydrocarbon transport in activated carbon is indeed due to surface diffusion.

Based on Eq. 13a, it is possible to estimate the magnitudes of the external film and intraparticle mass-transfer resistances. Figure 3d displays the fractions of the mass-transfer resistance due to external film and due to intraparticle mass transfer for the hydrocarbon-activated carbon system. This plot shows that, for the operating conditions used in the experiments, the film mass-transfer resistance is quite small and may be neglected for all practical purposes.

One of the main objectives of this research work is to derive a suitable relation for the LDF coefficient based on operating system variables. Since the transport mechanisms have been fully established in the foregoing analysis, it is now apparent that the LDF coefficient can be estimated based on Eqs. 13a and 14. Alternatively, with an average effective diffusivity, $D_{e,\text{ave}}$, and negligible external film resistance, the LDF coefficient can be related to the equilibrium constant as follows:

$$k = \left(\frac{15\epsilon_p D_{e,\text{ave}}}{R_p^2}\right)\left(\frac{C_{af}}{q^*\rho_p}\right). \tag{17}$$

In this case, $D_{e,\text{ave}}$, taken from Figure 3b, is 0.0085 cm^2/s. This equation is shown as a solid line in Figure 3a. Except for some deviation of propane data at higher concentrations, Eq. 17 provides a good estimate of the LDF coefficient over a wide range of operating conditions. This approach of correlating the LDF coefficient as a function of $(C_{af}/q^*\rho_p)$ by means of a constant average effective diffusivity is rather elegant and encouraging, as it provides a computationally convenient and reliable means of representing adsorption and desorption kinetics for the HC-AC system in dynamic process modeling, including pressure-swing-adsorption system simulations.

The average diffusivity value, $D_{e,\text{ave}}$, of 0.0085 cm^2/s found here is comparable to the values found for light hydrocarbon adsorption in various types of activated carbon, as reported by a number of researchers. Hu and Do (1992) reported slightly larger diffusivity values for ethane in large-slab activated carbon, which are primarily macropore-diffusion controlled. Costa et al. (1985) reported an effective particle diffusivity for ethane in AC-40 of about 0.005 cm^2/s. Huang and Fair (1988) found effective particle diffusivities of, depending on the exact value of the equilibrium constant, approximately 0.007 cm^2/s and 0.008 cm^2/s for the adsorption of ethane and propane, respectively, on Witco JCX activated carbon. In all these studies, surface diffusion is significant in portraying mass transfer in the activated-carbon particles.

It is worth mentioning that, for the experimental operating conditions chosen in this study, the mass-transfer Peclet number, P_{em}, calculated using Eq. 10 was reasonably high ($\sim$ 250 to 800), indicating that dispersion is not particularly significant. In any case, the interstitial gas velocity was varied for some of the experimental runs in order to study the accuracy of the correlation used to calculate the dispersion parameter. In this regard, the effective particle diffusivity found for a number of different gas velocities, with all other operating conditions remaining the same, were well within $\pm 20\%$ (Runs 1, 2, 6, 8, 9, 10, 11 for methane; Runs 2, 3, 5, 6 for ethane in Table 3). This indicated that the axial dispersion term was sufficiently accounted for in the simulations.

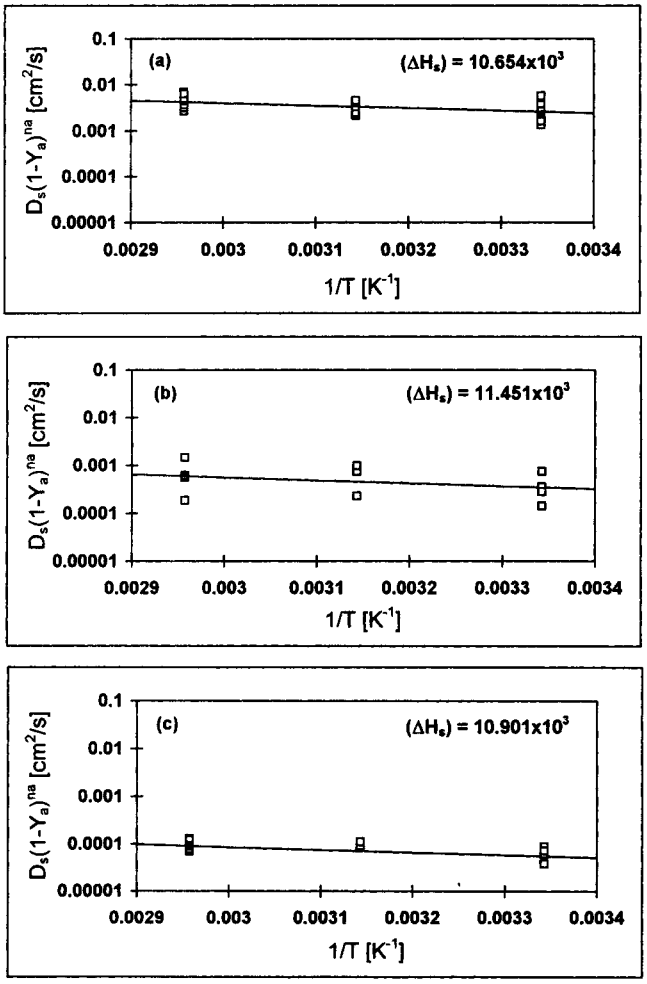

Figure 4. Semilogarithmic plots of $D_s(1-Y_a)^{na}$ as a function of $1/T$ for (a) methane, (b) ethane, and (c) propane.

See Tables 2 and 3 for relevant parameters; unit for (ΔH_s) is J/mol.

Kinetic data for hydrocarbon adsorption in silica gel (HC-SG)

For hydrocarbon adsorption in silica gel, Figure 5a shows the variation of the LDF coefficient with equilibrium constant, $(q^*\rho_p/C_{af})$. Here, a similar trend of decreasing LDF coefficient value by increasing equilibrium constant is obtained. The effective diffusivity for hydrocarbon adsorption in the silica gel as calculated using Eq. 13a for macropore control is shown in Figure 5b. In this case, the diffusivity val-

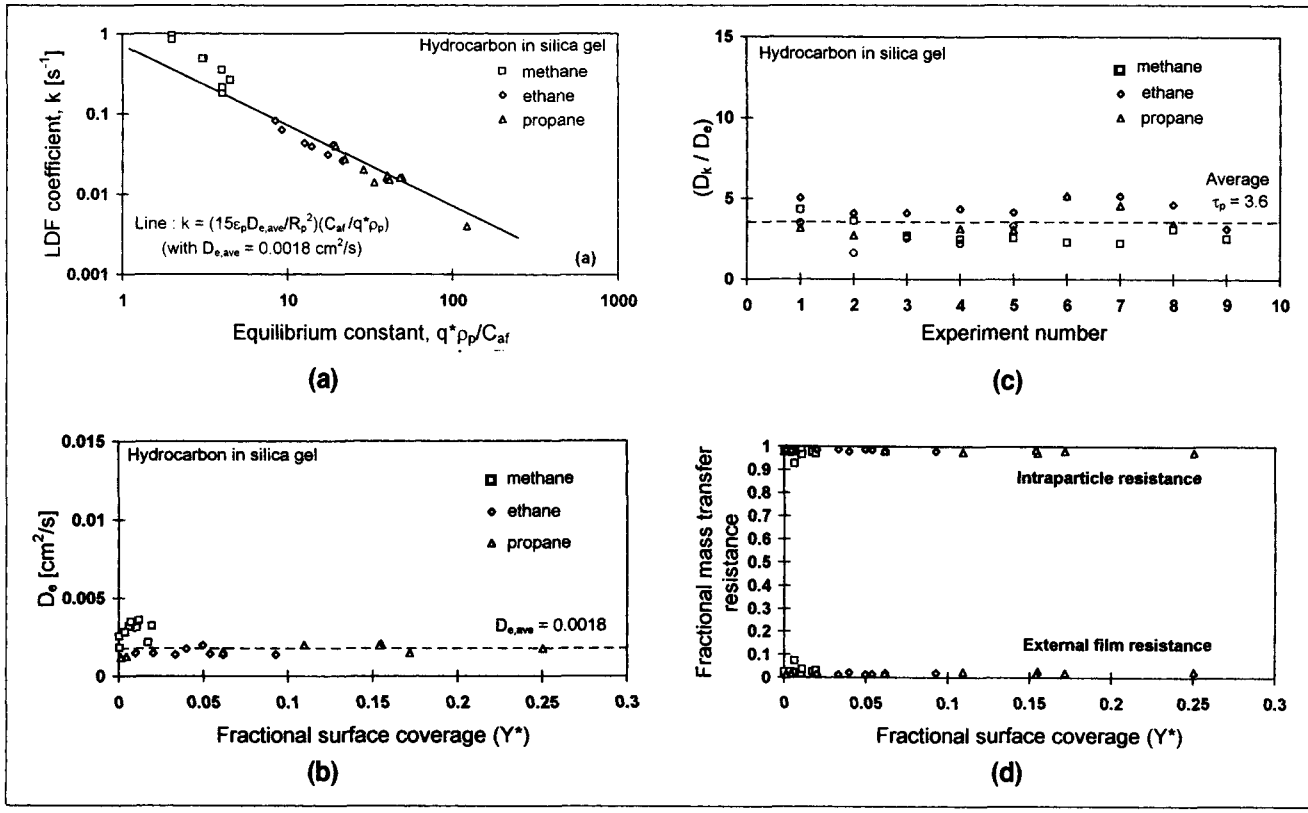

Figure 5. Mass-transfer kinetics of hydrocarbons in silica gel: (a) variation of LDF rate coefficient, k, with equilibrium constant; (b) variation of effective diffusivity, D_e, with surface coverage, Y_a; (c) (D_k/D_e) ratio for all the runs; (d) fraction of total particle mass-transfer resistance due to external film and intraparticle diffusion.

Experimental details are given in Tables 1 and 4.

ues are generally much lower than those found for hydrocarbon transport in activated carbon, with the average value being $D_{e,ave} = 0.0018$ cm^2/s. As with the HC-AC system, a plot of the ratio (D_k/D_e) for the HC-SG system is given in Figure 5c. In contrast to the HC-AC results, however, the average value of 3.6 found in this case is a physically realistic measure of the silica-gel particle tortuosity. This indicates that diffusion in the silica gel for all three hydrocarbons can be described well by Knudsen flow. In other words, the effective diffusivity, D_e, is given by

$$D_e = \left(\frac{D_k}{\tau_p}\right) \tag{14b}$$

with a particle tortuosity, $\tau_p = 3.6$. Table 4 shows the calculated diffusivities for the experimental runs conducted using silica gel as adsorbent.

As a further analysis, the fractions of mass-transfer resistance due to external film and intraparticle diffusion for silica gel is shown in Figure 5d. The figure shows that external film resistance is also negligible for the HC-SG system.

Mirroring the approach taken for correlating the LDF coefficient for hydrocarbon adsorption in activated carbon, Figure 5a shows the correlation line (Eq. 17) for HC-SG, using the average diffusivity value of 0.0018 cm^2/s. The correlation is indeed satisfactory. It should be noted that, since the particle diffusion appears to be controlled by Knudsen diffusion with a tortuosity value of 3.6, it is also possible to correlate the LDF coefficient for HC-SG as follows:

$$k = \left(\frac{15\epsilon_p D_k}{\tau_p R_p^2}\right)\left(\frac{C_{af}}{q^* \rho_p}\right) \tag{17a}$$

and adjust D_k in the simulation for each component according to the local temperature.

Heat-transfer data

Heat effects are very important in the hydrocarbon adsorption on activated carbon, but less so in silica gel. This is generally reflected in the heats of adsorption, $(-\Delta H_A)$, for the system as shown in Table 2. As a result of the significant amount of heat generation in these systems, it is necessary to take temperature variations in the bed into account. In the experimental setup used, two thermocouples were fitted in the adsorbent bed in order to measure the temperature profiles (Malek and Farooq, 1996a). Experimentally measured bed temperatures indicated temperature rises of 15°C for methane adsorption and about 45°C for ethane and propane adsorption in activated carbon.

Due to the high coolant flow rate in the column jacket, the experiment conducted here essentially approximates an

Table 4. Experimental and Calculated Mass-transfer Parameters for Hydrocarbon Adsorption on Silica Gel*

Run No.	T K	d_p** cm	X_f	Pres. bar	v_f cm/s	D_m cm^2/s	D_k cm^2/s	k s^{-1}	D_e cm^2/s	τ_p
					Methane					
1	299.15	0.258	0.006	3.9563	0.99	0.174	8.389E−03	0.180	1.847×10^3	4.33
2	299.15	0.258	0.167	5.4278	0.95	0.127	8.389E−03	0.210	2.173E−03	3.62
3	299.15	0.258	0.198	2.4848	1.74	0.278	8.389E−03	0.260	3.000E−03	2.71
4	299.15	0.258	0.207	4.9373	1.75	0.140	8.389E−03	0.350	3.655E−03	2.16
5	318.15	0.258	0.125	3.4658	0.87	0.221	8.651E−03	0.480	3.098E−03	2.69
6	318.15	0.258	0.160	5.4278	0.94	0.141	8.651E−03	0.480	3.293E−03	2.48
7	338.15	0.258	0.006	3.9563	0.99	0.214	8.919E−03	0.950	3.371E−03	2.54
8	338.15	0.258	0.123	3.4658	0.87	0.244	8.919E−03	0.850	3.758E−03	2.29
9	338.15	0.258	0.170	4.9373	1.03	0.171	8.919E−03	0.850	3.838E−03	2.21
					Ethane					
1	299.15	0.258	0.004	3.9563	0.90	0.132	6.126E−03	0.015	1.159E−03	5.05
2	299.15	0.258	0.151	3.4658	0.92	0.151	6.126E−03	0.026	1.437E−03	4.10
3	299.15	0.258	0.205	5.4278	0.91	0.096	6.126E−03	0.031	1.396E−03	4.13
4	299.15	0.258	0.227	2.4848	1.80	0.211	6.126E−03	0.041	1.906E−03	3.12
5	318.15	0.258	0.153	3.4658	0.92	0.168	6.318E−03	0.039	1.395E−03	4.36
6	318.15	0.258	0.200	5.4278	0.91	0.107	6.318E−03	0.043	1.436E−03	4.15
7	338.15	0.258	0.151	3.4658	0.91	0.186	6.513E−03	0.063	1.480E−03	4.25
8	338.15	0.258	0.207	5.4278	0.91	0.119	6.513E−03	0.082	1.775E−03	3.48
					Propane					
1	299.15	0.258	0.002	2.9753	1.01	0.143	5.058E−03	0.004	1.228E−03	3.98
2	299.15	0.258	0.138	3.9563	1.00	0.108	5.058E−03	0.016	2.052E−03	2.35
3	299.15	0.258	0.220	4.9373	1.00	0.086	5.058E−03	0.017	1.770E−03	2.70
4	299.15	0.258	0.225	2.4848	1.99	0.171	5.058E−03	0.016	1.945E−03	2.53
5	318.15	0.258	0.070	3.9563	1.00	0.120	5.217E−03	0.015	1.602E−03	3.12
6	318.15	0.258	0.224	4.9373	1.00	0.096	5.217E−03	0.020	1.477E−03	3.35
7	338.15	0.258	0.003	2.9753	1.01	0.177	5.378E−03	0.014	1.178E−03	4.43
8	338.15	0.258	0.138	3.9563	1.00	0.133	5.378E−03	0.027	1.538E−03	3.36
9	338.15	0.258	0.224	4.9373	1.00	0.106	5.378E−03	0.040	2.019E−03	2.54

*Adsorbent physical properties and other experimental details are given in Table 1.
**Particle size is mean of two Tyler Equivalent Mesh sizes (refer to Table 1).

isothermal-column wall condition. Experimentally measured coolant inlet and exit temperatures were essentially the same. As a further verification, Figure 6 shows a comparison of the bed temperature profile during adsorption for a constant wall temperature and a variable wall temperature. For the variable wall temperature, the (nondimensional) wall thermal balance at a particular axial location of the column is given by

$$\frac{\partial\theta_w}{\partial\tau} = \lambda_1[\,\delta_1(\theta_g-\theta_w)-\delta_2(\theta_w-\theta_f)] + \lambda_2\frac{\partial^2\theta_w}{\partial\chi^2}. \quad (18)$$

For the coolant flow rate used, the coolant-side heat-transfer coefficient, h_c, for annular flow was calculated to be approximately 1.6×10^{-2} W/cm^2 K (Geankoplis, 1993). The figure shows that the bed temperature profile is practically unaffected by the wall thermal dynamics, indicating negligible thermal resistance within the stainless-steel column wall.

The effective-wall heat-transfer coefficient was determined for each run based on fitting measured bed temperature profiles. Figure 7 shows a plot of the effective-wall Nusselt number, Nu_w [$=(h_w d_p)/K_g$], as a function of the Reynolds number, Re [$=(\rho_g\epsilon_B v_f d_p)/\mu$], for heat transfer from both the activated-carbon and silica-gel beds. The data cover experiments using all three gases and for controlled column-wall temperatures of 26°C, 45°C, and 65°C. It is clear that the wall Nu_w number is approximately constant (≈ 0.5) over the range of Re numbers studied here. In the nonisothermal breakthrough model used here, the apparent wall heat-transfer coefficient, h_w, adjusts for any model imperfection with respect to actual heat transfer in the bed. Hence, it can be expected to possess only a limited physical significance. Nevertheless, the values found here are of the same order of magnitude as the wall heat-transfer data presented by Freinwald and Paterson (1992) for air flowing in a packed bed of monosized ceramic spheres. The Nu_w values found here are lower than those predicted by Yagi and Kunii (1964) for flow in packed beds. This is to be expected since their model takes into account radial thermal dispersion, in addition to axial temperature gradients.

Multicomponent breakthrough

The mass- and heat-transfer kinetic parameters obtained from the single-component breakthrough experiments were used to simulate multicomponent breakthrough in the activated-carbon bed. In this case, two multicomponent breakthrough experiments were conducted with different operating conditions and feed concentrations of methane, ethane and propane. In the experiments conducted, samples of the exit gas from the adsorbent bed were taken at suitable time intervals and analyzed using a Perkin-Elmer Autosystem GC fitted with a TCD and a Supelco Carboxen-1004 Micropacked

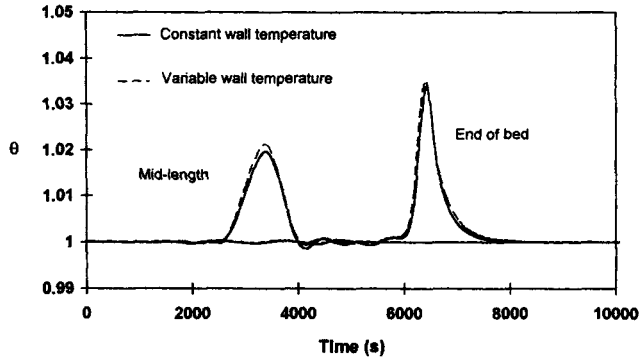

Figure 6. Effect of constant and variable column-wall temperature on the simulated-bed temperature profile as a function of time.

Column. Table 5 shows the operating conditions for the two multicomponent runs.

With regard to the simulation model, the only modification to the nonisothermal, nontrace model is the additional component balances for the gas and solid phases. The material and thermal-energy balances are as follows:

Component Material Balance

$$\frac{\partial X_k}{\partial \tau} = \frac{1}{P_{em}} \frac{\partial^2 X_k}{\partial \chi^2} - V \frac{\partial X_k}{\partial \chi} + \varphi \left(\frac{\partial Y_k}{\partial \tau} - X_k \sum_i \gamma_i \frac{\partial Y_i}{\partial \tau} \right). \quad (19)$$

Overall Material Balance

$$\frac{\partial V}{\partial \chi} = \frac{1}{P_{em}} \frac{2}{\theta^2} \left(\frac{\partial \theta}{\partial \chi} \right)^2 + \frac{V}{\theta} \frac{\partial \theta}{\partial \chi} - \varphi \sum_i \gamma_i \frac{\partial Y_i}{\partial \tau}. \quad (20)$$

Thermal-Energy Balance

$$\frac{\partial \theta}{\partial \tau} = \frac{1}{P_{eh}} \frac{\partial^2 \theta}{\partial \chi^2} - \phi_1 V \frac{\partial \theta}{\partial \chi} + \phi_1 \varphi \sum_i \left[\gamma_i (\theta + \zeta_i) \frac{\partial Y_i}{\partial \tau} \right] - \phi_2 (\theta - \theta_w). \quad (21)$$

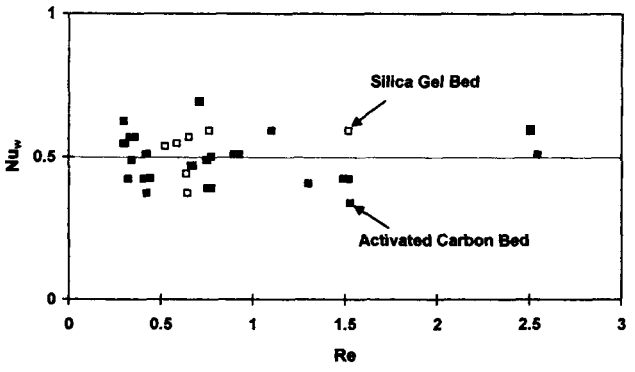

Figure 7. Column-wall Nusselt number as a function of gas Reynolds number for runs conducted in activated carbon and silica gel beds.

Table 5. Experimental Conditions, Kinetic, and Heat-Transfer Parameters Used in Multicomponent Breakthrough Simulations

Variable	Run MTC-1	Run MTC-2
Feed mole fraction		
X_{f1}	0.314	0.156
X_{f2}	0.123	0.157
X_{f3}	0.041	0.146
*LDF coefficient** [s^{-1}]		
k_1	0.290	0.260
k_2	0.045	0.050
k_3	0.009	0.013
h_w [J/cm²·s]	0.0025	0.0025
v_f [cm/s]	1.16	1.03
T_f [K]	299.15	299.15
P_B [bar]	2.583	2.583

*Calculated from Eq. 17.

Particle Mass-Transfer Equation is the LDF Equation

$$\frac{\partial Y_k}{\partial \tau} = \alpha_k (Y_k^* - Y_k). \quad (22)$$

The relevant boundary and initial conditions for the system are

$$\left. \frac{\partial X_k}{\partial \chi} \right|_{\chi=0} = -P_{em} (X_k|_{\chi=0^-} - X_k|_{\chi=0^+}) \quad (23a)$$

$$\left. \frac{\partial X_k}{\partial \chi} \right|_{\chi=1} = 0 \quad (23b)$$

$$V(0,\tau) = 1 \quad (23c)$$

$$\left. \frac{\partial V}{\partial \chi} \right|_{\chi=1} = 0 \quad (23d)$$

$$\left. \frac{\partial \theta}{\partial \chi} \right|_{\chi=0} = -P'_{eh} (\theta|_{\chi=0^-} - \theta|_{\chi=0^+}) \quad (23e)$$

$$\left. \frac{\partial \theta}{\partial \chi} \right|_{\chi=1} = 0 \quad (23f)$$

$$X_k(\chi,0) = 0, \qquad Y_k(\chi,0) = 0. \quad (23g)$$

In the model, it was assumed that there is no kinetic interaction between the three hydrocarbons for adsorption on the particles. The value of the LDF mass-transfer coefficient for each adsorbing component was calculated using Eq. 17, with the ratio $(C_{kf}/q^*\rho_p)$ computed based on the individual feed-gas concentrations. Two multicomponent equilibrium models were used for the purpose of comparison, namely, the extended Langmuir model and the extended Langmuir-Freundlich model. The Langmuir-Freundlich model was given in Eq. 8. The extended versions of the Langmuir and Langmuir-Freundlich isotherm models are as follows:

Extended Langmuir Model

$$Y_k^* = \frac{\beta_k X_k}{1 + \sum_i \beta_i X_i}, \tag{24}$$

where

$$\beta_k = b_{ok} \exp\left(\frac{(-\Delta H_A)_k}{RT_f}\frac{1}{\theta}\right) P_f.$$

Extended Langmuir-Freundlich Model

$$Y_k^* = \frac{\beta_k X_k^{nk}}{1 + \sum_i \beta_i X_i^{ni}}, \tag{25}$$

where

$$\beta_k = b_{ok} \exp\left(\frac{(-\Delta H_A)_k}{RT_f}\frac{1}{\theta}\right) P_f^{nk}.$$

Figure 8 shows the experimental and simulation breakthrough profiles for both the multicomponent equilibrium models. It is clear that while the extended Langmuir isotherm gives a reasonable agreement between the experimental profiles and the model predictions, a superior quantitative fit is obtained when the extended Langmuir-Freundlich isotherm is used. The better prediction obtained using the Langmuir-Freundlich model may be attributed to the following facts: the single-component kinetic parameters used in the multicomponent simulations were derived using this isotherm model and, compared to the Langmuir model, both the single- and multicomponent equilibrium data are better correlated using this isotherm model (Malek and Farooq, 1996b).

A notable difficulty in using the Langmuir-Freundlich model is the small negative gas-phase concentrations arising from oscillations in the numerical solution of the model. The oscillations are generally unavoidable due to the numerical method used in solving the mass and energy balances, particularly in the multicomponent breakthrough studies. The most effective way to proceed with negative gas-phase concentrations is to use its absolute value in the equilibrium calculations and then convert the equilibrium amount so calculated to a negative value if the gas-phase concentration is negative (Do, 1995). This ensures proper material balance in both the gas and solid phases. Since the oscillations in the gas-phase concentrations are normally very small, there is little observable difference in the computed breakthrough curves using this approach, as compared to assigning a zero value to negative gas-phase concentrations. Interestingly, however, the former approach leads to a more efficient computation, reducing the computation time appreciably. Nonetheless, the use of the extended Langmuir-Freundlich model incurs a higher computation time (approximately five times when performed on a Pentium 90-MHz personal computer) compared to using the extended Langmuir model. The appreciable difference is likely to be even greater in dynamic, multicomponent PSA simulations.

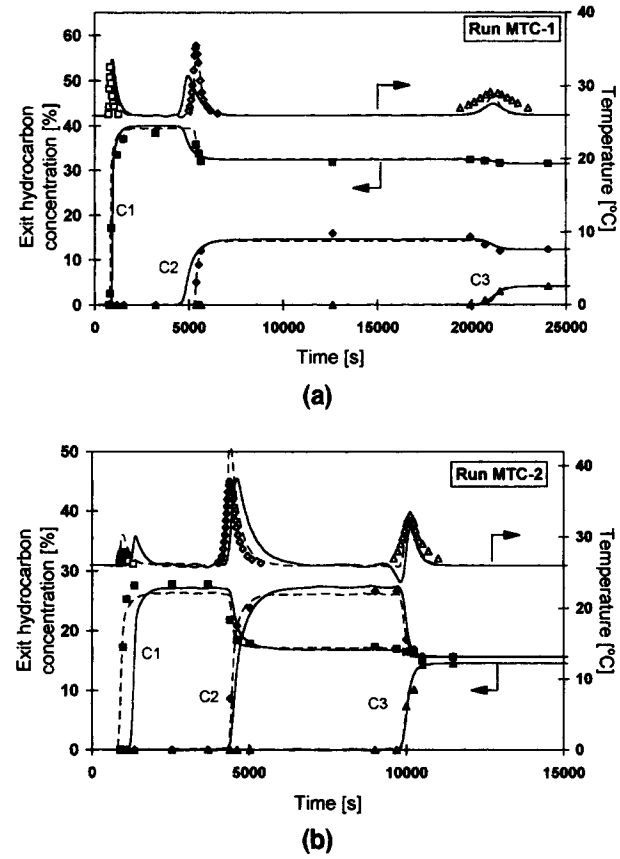

Figure 8. Experimental vs. theoretical multicomponent profiles for methane (C1), ethane (C2), and propane (C3) mixture adsorption in activated carbon.

Symbols, experimental; solid line, Langmuir model; dashed line, Langmuir-Freundlich model. Refer to Tables 1, 2 and 5 for equilibrium, kinetic, and other operating parameters.

Conclusions

The dynamic-column breakthrough method has been effectively used to determine both mass- and heat-transfer data for methane, ethane, and propane adsorption in activated-carbon and silica-gel beds. The advantage of this method over other gravimetric or volumetric experimental methods is that more representative data are obtained since a relatively large amount of adsorbent is used.

The LDF coefficient found for all three hydrocarbons in the activated-carbon adsorbent showed a monotonically decreasing trend with equilibrium constant. The effective particle diffusivity over the moderate range of operating conditions studied is approximately constant. Further analysis of the mass-transfer data shows that particle diffusion in the activated carbon is essentially through Knudsen and surface flow. In contrast to hydrocarbon adsorption in activated carbon, hydrocarbon diffusion in silica gel is controlled primarily by Knudsen flow. The experimental LDF coefficients for all three hydrocarbons are well correlated by the following simple equation:

$$k = \left(\frac{15\epsilon_p D_{e,\text{ave}}}{R_p^2}\right)\left(\frac{C_{af}}{q^*\rho_p}\right),$$

where $D_{e,ave}$ is 0.0085 cm^2/s for adsorption in activated carbon and $D_{e,ave}$ is 0.0018 cm^2/s for silica gel. The correlation covers the entire experimental range, which is adequate for the intended PSA operations. For both the adsorbents, the external-film mass-transfer resistance of the particle is less than 10% of total mass-transfer resistance, and may be neglected. Based on experimentally measured bed temperature profiles, the column-wall heat-transfer coefficient is also estimated. The results indicate that the effective column-wall Nusselt number is essentially constant (≈ 0.5) over the range of Reynolds numbers covered in this work.

It is further shown that multicomponent simulation using the single-component kinetic data and the extended Langmuir-Freundlich equilibrium isotherm provides excellent predictions of experimental breakthrough profiles. Although the quantitative agreement between theory and experiment is somewhat compromised if the extended Langmuir isotherm is used instead, the prediction is still reasonable and it accelerates the computation by more than five times. The gain in speed is certainly advantageous for PSA simulation and similar dynamic process modeling applications.

Notation

b_{ao} = constant in Langmuir-Freundlich equation, bar^{-1}
C = total gas-phase concentration in bed, mol/cm^3
C_{af} = gas-phase concentration of adsorbate in feed, mol/cm^3
$(C_p)_g$ = gas heat capacity, J/g·K
$(C_p)_s$ = particle heat capacity, J/g·K
d_p = mean particle diameter, cm
D_c = micropore diffusivity, cm^2/s
K = equilibrium constant, mmol/g·bar
K_g = axial gas-phase thermal conductivity, J/cm·s·K
K_p = particle thermal conductivity, J/cm·s·K
K_r = radial gas-phase thermal conductivity, J/cm·s·K
K_w = column-wall thermal conductivity, J/cm·s·K
K_{z0} = parameter defined by Eq. 12b, J/cm·s·K
L = column length, cm
M = molecular weight
P = pressure, bar
$P_e = (v_f d_p)/D_L$
$Pr = ([(C_p)_g \mu]/K_g)$, Prandtl number
q = adsorbed phase concentration, mmol/g
q^* = equilibrium adsorbed phase concentration, mmol/g
q_s^* = saturated equilibrium adsorbed phase concentration, mmol/g
R = universal gas constant (= 8.314 J/mol·K)
R_c = radius of microparticle, cm
R_i = column internal-wall radius, cm
R_o = column external-wall radius, cm
R_p = radius of macropore, cm
r_{po} = mean pore radius, cm
Sc = Schmidt number ($\mu D_m/\rho_g$)
T = temperature, K
t = time, s
v = velocity, cm/s
v_w = water velocity in column jacket, cm/s
$V = v/v_f$, dimensionless velocity
V_c = column volume, cm^3
X = dimensionless sorbate mole fraction in gas phase
$Y = q/q_s^*$, dimensionless solid-phase concentration
z = space dimension, cm

Greek letters

$\alpha = (Lk/v_f)$
$\chi = (z/L)$, dimensionless axial dimension
δ = constant used in Eq. 12a
$\delta_1 = 2R_i h_w$, J/cm·s·K
$\delta_2 = 2R_o h_c$, J/cm·s·K
ϵ = void fraction
$\phi_1 = [C(C_p)_g]/[C(C_p)_g + m\rho_p(C_p)_s]$
$\phi_2 = (2h_w L)/\{R_i v_f \epsilon_B[C(C_p)_g + m\rho_p(C_p)_s]\}$
$\gamma_i = q_{si}^*/q_{s1}^*$
$\varphi = [(1-\epsilon_B)/\epsilon_B](q_{s1}^*/C)\rho_p$
φ_1, φ_2 = constants used in Eq. 12c
$\lambda_1 = (L/v_w)\{1/[(R_o^2 - R_i^2)\rho_w(C_p)_w]\}$, cm·s·K
$\lambda_2 = K_w/[Lv_w\rho_w(C_p)_w]$, cm·s·K/J
μ = viscosity
$\theta = T/T_f$, dimensionless temperature
ρ = density, g/cm^3
$\tau = (v_f t/L)$, dimensionless time
$\zeta_a = [(-\Delta H_A)_a]/[(C_p)_g T_f]$

Superscripts and subscripts

na = exponent in single-component Langmuir-Freundlich isotherm
ni, nk = exponents in multicomponent Langmuir-Freundlich isotherm
1,2,3 = methane, ethane, and propane, respectively
B = adsorbent bed
e = bed exit conditions
f = feed or inlet conditions
g = gas phase
i, k = adsorbate components in multicomponent adsorption
o = initial conditions
p = particle
w = water in column jacket

Literature Cited

Bird, R. B., W. E. Stewart, and E. N. Lightfoot, *Transport Phenomena*, Wiley, New York (1960).

Costa, E., G. Callega, and F. Domingo, "Adsorption of Gaseous Hydrocarbons on Activated Carbon: Characteristic Kinetic Curve," *AIChE J.*, **31**(6), 982 (1985).

Do, D. D., Dept. of Chemical Engineering, University of Queensland, Australia, personal communication (November 1995).

Doong, S. J., and R. T. Yang, "Bulk Separation of Multicomponent Gas Mixtures by Pressure Swing Adsorption: Pore/Surface Diffusion and Equilibrium Models," *AIChE J.*, **32**(3), 397 (1986).

Edwards, M. F., and J. F. Richardson, "Gas Dispersion in Packed Beds," *Chem. Eng. Sci.*, **23**, 109 (1968).

Farooq, S., and D. M. Ruthven, "Heat Effects in Adsorption Column Dynamics. 1. Comparison of One- and Two-Dimensional Models," *Ind. Eng. Chem. Res.*, **29**(6), 1076 (1990).

Finlayson, B. A., *The Method of Weighted Residuals and Variational Principles*, Academic Press, New York (1972).

Freinwald, M. G., and W. R. Paterson, "Accuracy of Model Predictions and Reliability of Experimental Data for Heat Transfer in Packed Beds," *Chem. Eng. Sci.*, **47**(7), 1545 (1992).

Garg, D. R., and D. M. Ruthven, "The Effect of the Concentration Dependence of Diffusivity on Zeolitic Sorption Curves," *Chem. Eng. Sci.*, **27**, 417 (1972).

Garg, D. R., and D. M. Ruthven, "Linear Driving Force Approximations for Diffusion Controlled Adsorption in Molecular Sieve Columns," *AIChE J.*, **21**(1), 200 (1975).

Geankoplis, C. J., *Transport Processes and Unit Operations*, 3rd ed., Prentice-Hall, Englewood Cliffs, NJ (1993).

Hu, X., and D. D. Do, "Multicomponent Adsorption Kinetics of Hydrocarbons onto Activated Carbon: Effect of Adsorption Equilibrium Equations," *Chem. Eng. Sci.*, **47**(7), 1715 (1992).

Hu, X., and D. D. Do, "Multicomponent Adsorption Kinetics of Hydrocarbons onto Activated Carbon: Contribution of Micropore Resistance," *Chem. Eng. Sci.*, **48**(7), 1317 (1993).

Huang, C. C., and J. R. Fair, "Study of the Adsorption and Desorption of Multiple Adsorbates in a Fixed Bed," *AIChE J.*, **34**(11), 1861 (1988).

Kapoor, A., R. T. Yang, and C. Wong, "Surface Diffusion," *Catal. Rev. Sci. Eng.*, **31**(1&2), 129 (1989).

Karger, J., and D. M. Ruthven, *Diffusion in Zeolites and Other Microporous Solids*, Wiley, New York (1992).

Kunii, D., and J. M. Smith, "Heat Transfer Characteristics of Porous Rocks," *AIChE J.*, **6**, 71 (1960).
Malek, A., S. Farooq, M. N. Rathor, and K. Hidajat, "Effect of Velocity Variation due to Adsorption-Desorption on Equilibrium Data from Breakthrough Experiments," *Chem. Eng. Sci.*, **50**, 737 (1995).
Malek, A., and S. Farooq, "Determination of Equilibrium Isotherms Using Dynamic Column Breakthrough and Constant Flow Equilibrium Desorption," *J. Chem. Eng. Data*, **41**, 25 (1996a).
Malek, A., and S. Farooq, "Comparison of Isotherm Models for Hydrocarbon Adsorption on Activated Carbon," *AIChE J.*, **42**(11), 3191 (1996b).
Malek, A., "A Study of Hydrogen Purification from the Refinery Fuel Gas by Pressure Swing Adsorption," PhD Thesis, Dept. of Chemical Engineering, National Univ. of Singapore (1996).
Press, W. H., S. A. Teukolsky, W. T. Vetterling, and B. P. Flannery, *Numerical Recipes in FORTRAN*, 2nd ed., Cambridge Univ. Press, New York (1992).
Raghavan, N. S., and D. M. Ruthven, "Numerical Simulation of a Fixed Bed Adsorption Column by the Method of Orthogonal Collocation," *AIChE J.*, **29**(6), 922 (1983).
Ruthven, D. M., *Principles of Adsorption and Adsorption Processes*, Wiley, New York (1984).
Ruthven, D. M., S. Farooq, and K. S. Knaebel, *Pressure Swing Adsorption*, VCH Publishers, New York (1994).
Suzuki, M., *Adsorption Engineering*, Elsevier, Amsterdam, p. 193 (1990).
Tsai, M. C., S. S. Wang, and R. T. Yang, "Pore-diffusion Model for Cyclic Separation: Temperature Swing Separation of Hydrocarbon and Methane at Elevated Pressures," *AIChE J.*, **29**(6), 966 (1983).
Vermeulen, T., "Theory for Irreversible and Constant-Pattern Solid Diffusion," *Ind. Eng. Chem.*, **45**, 1664 (1953).
Vermeulen, T., and R. E. Quilici, "Analytic Driving-Force Relation for Pore Diffusion Kinetics in Fixed-Bed Adsorption," *Ind. Eng. Chem. Fundam.*, **9**, 179 (1970).
Wakao, N., and T. Funarzkri, "Effect of Fluid Dispersion Coefficients on Particle-to-Fluid Mass Transfer Coefficients in Packed Bed," *Chem. Eng. Sci.*, **33**, 1375 (1978).
Yagi, S., D. Kunii, and N. Wakao, "Studies on Axial Effective Thermal Conductivities in Packed Beds," *AIChE J.*, **6**(4), 543 (1960).
Yagi, S., and D. Kunii, "Studies on Heat Transfer Near Wall Surface in Packed Beds," *AIChE J.*, **6**(1), 97 (1964).

Appendix: Derivation and Solution of the Breakthrough Model

For a multicomponent adsorption flow process in a packed bed of adsorbent, the material balance for component k as given by the axial dispersed plug-flow model is as follows:

$$-\frac{\partial C_k}{\partial t} = -D_L\frac{\partial^2 C_k}{\partial z^2} + \frac{\partial \upsilon C_k}{\partial z} + \frac{1-\epsilon_B}{\epsilon_B}\rho_p\frac{\partial q_k}{\partial t}, \quad \text{(A1)}$$

with Danckwerts boundary conditions

$$D_L\frac{\partial C_k}{\partial z}\bigg|_{z=0} = -\upsilon_f(C_k|_{z=0^-} - C_k|_{z=0^+}) \quad \text{(A2a)}$$

$$\frac{\partial C_k}{\partial z}\bigg|_{z=L} = 0. \quad \text{(A2b)}$$

Assuming that ideal gas law applies for the gas-phase, Eq. A1 can be expanded for a nonisothermal, isobaric process to give

$$\frac{\partial X_k}{\partial t} = D_L\left(\frac{\partial^2 X_k}{\partial z^2} - \frac{2}{T}\frac{\partial X_k}{\partial z}\frac{\partial T}{\partial z} + \frac{2X_k}{T^2}\left(\frac{\partial T}{\partial z}\right)^2 - \frac{X_k}{T}\frac{\partial^2 T}{\partial z^2}\right) - \left(\upsilon\frac{\partial X_k}{\partial z} + X_k\frac{\partial \upsilon}{\partial z} - \frac{\upsilon X_k}{T}\frac{\partial T}{\partial z}\right) + \frac{X_k}{T}\frac{\partial T}{\partial t} - \frac{1}{C}\frac{1-\epsilon_B}{\epsilon_B}\rho_p\frac{\partial q_k}{\partial t}, \quad \text{(A3)}$$

where $C = (P/RT) = f(T)$.

The total material balance is given by

$$0 = D_L\left(\frac{2}{T^2}\left(\frac{\partial T}{\partial z}\right)^2 - \frac{1}{T}\frac{\partial^2 T}{\partial z^2}\right) - \left(\frac{\partial \upsilon}{\partial z} - \frac{\upsilon}{T}\frac{\partial T}{\partial z}\right) + \frac{1}{T}\frac{\partial T}{\partial t} - \frac{1}{C}\frac{1-\epsilon_B}{\epsilon_B}\rho_p\sum_i\frac{\partial q_i}{\partial t}$$

or

$$\frac{\partial \upsilon}{\partial z} = D_L\left(\frac{2}{T^2}\left(\frac{\partial T}{\partial z}\right)^2 - \frac{1}{T}\frac{\partial^2 T}{\partial z^2}\right) + \frac{\upsilon}{T}\frac{\partial T}{\partial z} + \frac{1}{T}\frac{\partial T}{\partial t} - \frac{1}{C}\frac{1-\epsilon_B}{\epsilon_B}\rho_p\sum_i\frac{\partial q_i}{\partial t}, \quad \text{(A4)}$$

with boundary condition

$$\upsilon(0,t) = \upsilon_f. \quad \text{(A5)}$$

An energy balance for the system, with axial thermal conduction and constant wall temperature, yields

$$(1-\epsilon_B)\rho_p(C_p)_s\frac{\partial T}{\partial t} = K_z\frac{\partial^2 T}{\partial z^2} - \epsilon_B C T(C_p)_g\frac{\partial \upsilon}{\partial z} - (1-\epsilon_B)\rho_p\sum_i(-\Delta H_A)_i\frac{\partial q_i}{\partial t} - \frac{2h_w}{R_B}(T-T_w). \quad \text{(A6)}$$

The boundary condition for the energy balance is similar to the Danckwerts condition for mass balance as follows:

$$K_z\frac{\partial T}{\partial z}\bigg|_{z=0} = -\upsilon_f C(C_p)_g(T|_{z=0^-} - T|_{z=0^+}) \quad \text{(A7a)}$$

$$\frac{\partial T}{\partial z}\bigg|_{z=1} = 0. \quad \text{(A7b)}$$

Combining Eqs. A3 and A4 gives the following transient material balance for the gas-phase concentration in dimensionless form

$$\frac{\partial X_k}{\partial \tau} = \frac{1}{P_{em}}\left(\frac{\partial^2 X_k}{\partial \chi^2} - \frac{2}{\theta}\frac{\partial X_k}{\partial \chi}\frac{\partial \theta}{\partial \chi}\right) - V\frac{\partial X_k}{\partial \chi} + \varphi\left(\frac{\partial Y_k}{\partial \tau} - X_k\sum_i\gamma_i\frac{\partial Y_i}{\partial \tau}\right) \quad \text{(A8)}$$

$$\frac{\partial V}{\partial \chi} = \frac{1}{P_{em}}\left(\frac{2}{\theta^2}\left(\frac{\partial \theta}{\partial \chi}\right)^2 - \frac{1}{\theta}\frac{\partial^2 \theta}{\partial \chi^2}\right) + \frac{1}{\theta}\frac{\partial \theta}{\partial \tau} + \frac{V}{\theta}\frac{\partial \theta}{\partial \chi} - \varphi \sum_i \gamma_i \frac{\partial Y_i}{\partial \tau}. \quad \text{(A9)}$$

Combining Eqs. A6 and A4, the nondimensional energy balance is, in turn, given by

$$\frac{\partial \theta}{\partial \tau} = \left(\frac{1}{P_{eh}} + \frac{\phi_1}{P_{em}}\right)\frac{\partial^2 \theta}{\partial \chi^2} - \phi_1 V \frac{\partial \theta}{\partial \chi} - \frac{2\phi_1}{P_{em}}\frac{1}{\theta}\left(\frac{\partial \theta}{\partial \chi}\right)^2 + \phi_1 \varphi \sum_i \left(\gamma_i(\theta + \zeta_i)\frac{\partial Y_i}{\partial \tau}\right) - \phi_2(\theta - \theta_w). \quad \text{(A10)}$$

The boundary conditions are as follows:

$$\left.\frac{\partial X_k}{\partial \chi}\right|_{\chi=0} = -P_{em}(X_k|_{\chi=0^-} - X_k|_{\chi=0^+}) \quad \text{(A11a)}$$

$$\left.\frac{\partial X_k}{\partial \chi}\right|_{\chi=1} = 0 \quad \text{(A11b)}$$

$$V(0,\tau) = 1 \quad \text{(A11c)}$$

$$\left.\frac{\partial \theta}{\partial \chi}\right|_{\chi=0} = -P'_{eh}(\theta|_{\chi=0^-} - \theta|_{\chi=0^+}) \quad \text{(A11d)}$$

$$\left.\frac{\partial \theta}{\partial \chi}\right|_{\chi=1} = 0. \quad \text{(A11e)}$$

The particle uptake equation represented by the linear driving-force approximation and the equilibrium isotherm expression completes the breakthrough model. For a single sorbate system, the summation terms in Eqs. A8, A9 and A10 are not required, giving the following expressions instead:

$$\frac{\partial X_a}{\partial \tau} = \frac{1}{P_{em}}\left(\frac{\partial^2 X_a}{\partial \chi^2} - \frac{2}{\theta}\frac{\partial X_a}{\partial \chi}\frac{\partial \theta}{\partial \chi}\right) - V\frac{\partial X_a}{\partial \chi} + \varphi(X_a - 1)\frac{\partial Y_a}{\partial \tau} \quad \text{(A8a)}$$

$$\frac{\partial V}{\partial \chi} = \frac{1}{P_{em}}\left(\frac{2}{\theta^2}\left(\frac{\partial \theta}{\partial \chi}\right)^2 - \frac{1}{\theta}\frac{\partial^2 \theta}{\partial \chi^2}\right) + \frac{1}{\theta}\frac{\partial \theta}{\partial \tau} + \frac{V}{\theta}\frac{\partial \theta}{\partial \chi} - \varphi\frac{\partial Y_a}{\partial \tau} \quad \text{(A9a)}$$

$$\frac{\partial \theta}{\partial \tau} = \left(\frac{1}{P_{eh}} + \frac{\phi_1}{P_{em}}\right)\frac{\partial^2 \theta}{\partial \chi^2} - \phi_1 V \frac{\partial \theta}{\partial \chi} - \frac{2\phi_1}{P_{em}}\frac{1}{\theta}\left(\frac{\partial \theta}{\partial \chi}\right)^2 + \phi_1 \varphi(\theta + \zeta_a)\frac{\partial Y_a}{\partial \tau} - \phi_2(\theta - \theta_w). \quad \text{(A10a)}$$

Discernibly, the breakthrough model given earlier comprises a set of partial differential equations. In the solution scheme adopted in this study, these equations are discretized in the spatial dimension to generate a set of time-derivative ordinary differential equations. The discretization is done using the method of orthogonal collocation.

Manuscript received Aug. 7, 1996, and revision received Nov. 4, 1996.